

2-D Rayleigh Autoregressive Moving Average Model for SAR Image Modeling

B. G. Palm*

F. M. Bayer[†]R. J. Cintra[‡]

Abstract

Two-dimensional (2-D) autoregressive moving average (ARMA) models are commonly applied to describe real-world image data, usually assuming Gaussian or symmetric noise. However, real-world data often present non-Gaussian signals, with asymmetrical distributions and strictly positive values. In particular, SAR images are known to be well characterized by the Rayleigh distribution. In this context, the ARMA model tailored for 2-D Rayleigh-distributed data is introduced—the 2-D RARMA model. The 2-D RARMA model is derived and conditional likelihood inferences are discussed. The proposed model was submitted to extensive Monte Carlo simulations to evaluate the performance of the conditional maximum likelihood estimators. Moreover, in the context of SAR image processing, two comprehensive numerical experiments were performed comparing anomaly detection and image modeling results of the proposed model with traditional 2-D ARMA models and competing methods in the literature.

Keywords

Anomaly detection, ARMA modeling, Rayleigh distribution, SAR images, two-dimensional models

1 Introduction

The parametric representation of two-dimensional homogeneous random fields considering two-dimensional (2-D) autoregressive moving average (ARMA) models is frequently adopted for image processing [Bustos et al., 2009a, Kizilkaya and Kayran, 2005, Ojeda et al., 2010, Bustos et al., 2009b], including (i) modeling [Bustos et al., 2009a, Rosenfeld, 2014]; (ii) compression [Nijim et al., 1996]; (iii) encoding [Chung and Kanefsky, 1992]; and (iv) restoration [Lim, 1990, Vallejos and Mardesic, 2004]. The 2-D ARMA model is an spatial extension of the classical one-dimensional (1-D) ARMA model [Brockwell and Davis, 2016], and it is often employed in edge detection [Ojeda et al., 2010] and stochastic texture analysis [Hall and Giannakis, 1995].

In particular, the two-dimensional autoregressive first-order model is commonly applied to describe real-world image data [Kashyap and Eom, 1988, Bennett and Khotanzad, 1999], representing different types of textures [Bustos et al., 2009b]. Theoretical details of the two-dimensional autoregressive first-order model, such as properties, correlation structure, and maximum likelihood estimators of the parameters can be found in Basu and Reinsel [1993]. The ARMA model is preferable over the autoregressive (AR) and moving average (MA) model, since it provides more effective models for homogeneous random fields [Cadzow and Ogino, 1981, Zhang, 1991]. In fact, ARMA models can better characterize the power in the spectral domain representation when compared to AR or MA models [Kizilkaya and Kayran, 2005].

ARMA modeling usually assumes Gaussian or symmetric noise distribution, incurring inferential problems when this assumption is not satisfied [Kizilkaya and Kayran, 2005, Zoubir et al., 2018, Wegman et al., 1989]. Indeed, the Gaussianity hypothesis has been widely considered in statistical signal processing [Zoubir et al., 2018], remote sensing analysis [Zhao et al., 2008, 2016, Morales-Alvarez et al., 2017], and detection theory [Kay, 2000, Xue et al., 2020, Wang et al., 2019]. However, actual measured signals often present non-Gaussian properties [Margoosian et al., 2015, Liu et al., 2018], such as asymmetrical distributions and strictly positive values.

*Department of Mathematics and Natural Sciences, Blekinge Institute of Technology, Sweden; Programa de Pós-graduação em Estatística, Universidade Federal Pernambuco, Brazil; Signal Processing Group, Departamento de Estatística, Universidade Federal Pernambuco, Brazil. E-mail: bruna.palm@bth.se

[†]Departamento de Estatística and LACESM, Universidade Federal de Santa Maria, Brazil. E-mail: bayer@ufsm.br

[‡]Signal Processing Group, Departamento de Estatística, Universidade Federal Pernambuco, Brazil; School of Science and Mathematics, Howard Payne University, Texas, USA. E-mail: rjds@de.ufpe.br

An alternative approach for modeling such type of data is the use of the Rayleigh distribution [Bayer et al., 2020a]. This model is considered in signal and image processing [Zanetti et al., 2015, Sumaiya and Kumari, 2018], being relevant in the context of synthetic aperture radar (SAR) image modeling, due to its good characterization of image pixel amplitude values [Yue et al., 2019, Kuruoglu and Zerubia, 2004, Jackson and Moses, 2009, Kuttikkad and Chellappa, 2000]. In particular, this distribution is known to well fit SAR data homogeneous regions [Oliver and Quegan, 2004, Yue et al., 2021]. The main justification for supposing the Rayleigh distribution as a model for the amplitude of SAR data is that the assumption of a large number of reflectors in an observed image allows one to invoke the central limit theorem, according to which the distribution of the real and complex parts of the received signal are independent and approaches the Gaussian distribution with zero mean and constant variance [Kuruoglu and Zerubia, 2004, Yue et al., 2021]. Thus, under these assumptions, the amplitude values of complex SAR data are exactly Rayleigh distributed.

Frequently, the SAR image modeling is performed assuming constant parameters [Kuruoglu and Zerubia, 2004, Jackson and Moses, 2009]. In cases where this assumption is not suitable, an alternative is to use a regression model, where each observation has one specific estimated mean [Wang and Ouchi, 2008, McCullagh and Nelder, 1989, Palm et al., 2019]. Motivated by these SAR image characteristics, Palm et al. [2019] proposed a regression model based on the Rayleigh distribution for SAR image modeling. However, image pixels usually present a resolution spatial dependence [Jackson and Moses, 2009, Yan et al., 2018], and consequently, a 2-D model can be used as a venue for addressing such a problem.

The use of one- or two-dimensional dynamical models are often employed in image applications. For example, in Almeida-Junior and Nascimento [2021], the authors proposed a new 1-D ARMA model considering the \mathcal{G}_0 distribution to estimate the intensity values of SAR image pixels. Bayer et al. [2020a] derived an 1-D Rayleigh-based dynamical model useful to land-use classification in SAR images. In Bustos et al. [2009b], a 2-D Gaussian ARMA model was applied in image filtering schemes. Additionally, the literature presents several studies for 1-D dynamical models based on different distributions, useful in a multitude of scientific applications; see., e.g., Benjamin et al. [2003], Bayer et al. [2017], Rocha and Cribari-Neto [2009], Möller and Weiß [2020], Palm et al. [2021].

However, to the best of our knowledge, a two-dimensional ARMA model assuming the Rayleigh distribution is not present in the literature and this paper aims at proposing a first treatment on the topic. Our goal is two-fold. First, we derive a two-dimensional ARMA model for non-Gaussian spatial autocorrelated images, where the observed signal is asymmetric and strictly positive. For the proposed model, we introduce parameter estimation, large data record inference, and the quantile residuals. Second, we propose an image modeling tool based on the derived spatial model estimated parameters and an anomaly detector for non-Gaussian SAR images. Considering control charts of the proposed model residuals, the introduced detection scheme measures the deviations of an observed pixel value from its estimated mean value. The residual-based control charts have already been employed in remote sensing data change and anomaly detection [Bayer et al., 2020b, Brooks et al., 2013].

Anomaly detection is a popular field in signal processing, machine learning, and statistics [Talagala et al., 2020, Kadri et al., 2016, Quatrini et al., 2020, Kwon and Nasrabadi, 2005]. In particular, anomaly detection in noisy image is explored for quality control purposes in different manufacturing applications, such as composites, steel, and textile production [Yan et al., 2018]. The anomaly detection problem can be addressed considering different techniques, depending on the way that anomalies are defined. For example, different types of expected outputs or input data have particular problem formulation and need to be addressed through specific techniques [Talagala et al., 2020]. On the other hand, our proposal is based on a simple residual analyze considering control chart with a fixed theoretical threshold, which is defined based on the residual distribution.

This paper is organized as follows. In Section 2, we describe the proposed spatial model, provide conditional maximum likelihood estimators, and present a hypothesis testing methodology. Section 3 details the introduced image modeling tool and proposed an anomaly detection algorithm. Section 4 presents Monte Carlo simulations and two empirical analyses of the derived detector applied to SAR images. Section 5 brings final remarks and concludes the paper.

2 The Proposed Model

2.1 Mathematical Setup

Recently, a regression model [Palm et al., 2019] and an 1-D ARMA model [Bayer et al., 2020a] based on the Rayleigh distribution have been proposed. The Rayleigh ARMA (RARMA) model introduced in Bayer et al. [2020a] relates the mean of an one-dimensional discrete-time signal to a linear predictor through a strictly monotonic, twice differentiable link function $g(\cdot)$, where $g : \mathbb{R}^+ \rightarrow \mathbb{R}$. The goal of this section is to extend the 1-D model presented in Bayer et al. [2020a] and introduce to the 2-D case.

Let $Y[n, m]$, $n = 1, 2, \dots, N$, $m = 1, 2, \dots, M$, be a random variable representing the pixels of an $N \times M$ image; and let $y[n, m]$ be the realization of the signal $Y[n, m]$. Additionally, let $S[n, m] = \{[k, l] \in \mathbb{Z}^2 : 1 \leq k \leq n, 1 \leq l \leq m\} - \{[n, m]\}$ be the strongly causal region at $[n, m]$ [Bustos et al., 2009b]. Assume that, conditionally to the information set in the neighborhood $S[n, m]$, each $Y[n, m]$ is distributed according to the Rayleigh distribution. Considering the mean-based parametrization of $Y[n, m]$ propose in Palm et al. [2019], we have that the conditional density of $Y[n, m]$, given $S[n, m]$, is provided by

$$f_Y(y[n, m] | S[n, m]) = \frac{\pi y[n, m]}{2\mu[n, m]^2} \exp\left(-\frac{\pi y[n, m]^2}{4\mu[n, m]^2}\right),$$

where $\mu[n, m] > 0$. The cumulative distribution function is given by

$$F_Y(y[n, m] | S[n, m]) = 1 - \exp\left(-\frac{\pi y[n, m]^2}{4\mu[n, m]^2}\right).$$

The conditional mean and conditional variance of $Y[n, m]$, given $S[n, m]$, are, respectively, expressed by means of

$$\begin{aligned} E(Y[n, m] | S[n, m]) &= \mu[n, m], \\ \text{Var}(Y[n, m] | S[n, m]) &= \mu[n, m]^2 \left(\frac{4}{\pi} - 1\right). \end{aligned}$$

2.2 The Model

The proposed 2-D Rayleigh autoregressive and moving average model, hereafter referred to as 2-D RARMA, is defined according to

$$\Phi(z_1, z_2)g(y[n, m]) = \beta + \Theta(z_1, z_2)e[n, m], \quad (1)$$

where the two-dimensional autoregressive operator $\Phi(z_1, z_2)$ and moving average operator $\Theta(z_1, z_2)$ are furnished, respectively, by

$$\begin{aligned} \Phi(z_1, z_2) &= 1 - \sum_{i=0}^p \sum_{j=0}^p \phi_{(i, j)} z_1^i z_2^j, \\ \Theta(z_1, z_2) &= 1 + \sum_{k=0}^q \sum_{l=0}^q \theta_{(k, l)} z_1^k z_2^l, \end{aligned}$$

and $\beta \in \mathbb{R}$ is an intercept; the quantities $z_1^i g(y[n, m]) = g(y[n - i, m])$, $z_2^j g(y[n, m]) = g(y[n, m - j])$, $z_1^k e[n, m] = e[n - k, m]$, and $z_2^l e[n, m] = e[n, m - l]$ are the backward operators; p and q are the orders of the model; the quantities $\phi_{(i, j)}$, $i, j = 0, 1, \dots, p$, and $\theta_{(k, l)}$, $k, l = 0, 1, \dots, q$, are, respectively, the autoregressive and moving average parameters estimated based on the image pixels; $e[n, m] = g(y[n, m]) - g(\mu[n, m])$ is the moving average error term; and $g(\mu[n, m]) = \eta[n, m]$ the linear predictor. As suggested in Basu and Reinsel [1993] for an unilateral spatial ARMA, we assume $\phi_{(0,0)} = \theta_{(0,0)} = 0$. Replacing the

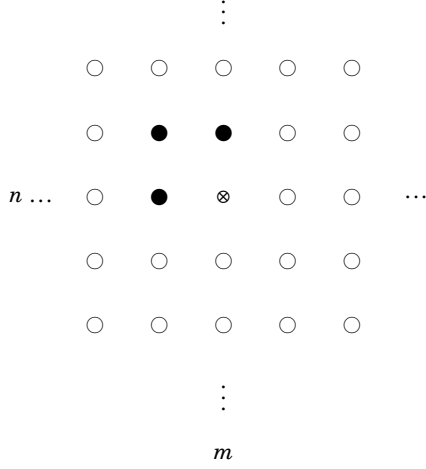


Figure 1: Example of the neighborhood used in a 2-D RARMA(1,1) model.

quantities described above in (1), the 2-D RARMA (p,q) model can be rewritten as

$$g(\mu[n,m]) = \beta + \sum_{i=0}^p \sum_{j=0}^p \phi_{(i,j)} g(y[n-i, m-j]) + \sum_{k=0}^q \sum_{l=0}^q \theta_{(k,l)} e[n-k, m-l]. \quad (2)$$

Figure 1 depicts the considered neighbors pixels in a 2-D RARMA(1,1) model.

As in 1-D non-Gaussian dynamical models considering conditional probability models under different distributions, conditions of weak stationarity, causality, and invertibility are still challenging and open topics in the literature. This limitation is related to the fact that, for link functions other than the identity, the MA error terms are not martingale differences, which make the first two moments of the marginal distribution intractable [Benjamin et al., 2003]. However, this fact does not make such models less useful in practice, being widely used in different areas of knowledge, see, e.g., Melchior et al. [2021], Almeida-Junior and Nascimento [2021], Leiva et al. [2020], Rothermel et al. [2020], Liboschik et al. [2017], Scher et al. [2020].

2.3 Conditional Likelihood Estimation

The estimation of the 2-D RARMA (p,q) model parameters can be realized by maximizing the logarithm of the conditional likelihood function [Brockwell and Davis, 2016]. Let $\gamma = (\beta, \phi^\top, \theta^\top)^\top$ be the parameter vector where $\phi = (\phi_{(0,1)}, \phi_{(0,2)}, \dots, \phi_{(p,p)})^\top$ and $\theta = (\theta_{(0,1)}, \theta_{(0,2)}, \dots, \theta_{(q,q)})^\top$, with dimensions $(p+1)^2 - 1$ and $(q+1)^2 - 1$, respectively. The log-likelihood function for γ , conditional to the $w = \max(p,q)$ preliminary observations, is given by

$$\ell(\gamma) = \sum_{n=w+1}^N \sum_{m=w+1}^M \log f_Y(y[n,m] | S[n,m]) = \sum_{n=w+1}^N \sum_{m=w+1}^M \ell[n,m](\mu[n,m]),$$

where

$$\ell[n,m](\mu[n,m]) = \log\left(\frac{\pi}{2}\right) + \log(y[n,m]) - \log(\mu[n,m]^2) - \frac{\pi y[n,m]^2}{4\mu[n,m]^2}.$$

The conditional maximum likelihood estimator (CMLE), $\hat{\gamma}$, can be obtained by solving

$$\mathbf{U}(\gamma) = \frac{\partial \ell}{\partial \gamma^\top} = \left(\frac{\partial \ell}{\partial \beta}, \frac{\partial \ell}{\partial \phi^\top}, \frac{\partial \ell}{\partial \theta^\top} \right)^\top = \mathbf{0}, \quad (3)$$

where $\mathbf{U}(\gamma)$ is the score vector and $\mathbf{0}$ is the vector of zeros with dimension $(p+1)^2 + (q+1)^2 - 1$. Computing the derivatives in (3), we obtain

$$\frac{\partial \ell}{\partial \gamma} = \sum_{n=w+1}^N \sum_{m=w+1}^M \frac{\partial \ell[n,m](\mu[n,m])}{\partial \mu[n,m]} \frac{d\mu[n,m]}{d\eta[n,m]} \frac{\partial \eta[n,m]}{\partial \gamma}.$$

Note that $\frac{d\ell[n,m](\mu[n,m])}{d\mu[n,m]} = \frac{\pi y[n,m]^2}{2\mu[n,m]^3} - \frac{2}{\mu[n,m]}$ and $\frac{d\mu[n,m]}{d\eta[n,m]} = \frac{1}{g'(\mu[n,m])}$, where $g'(\cdot)$ is the first derivative of the selected link function $g(\cdot)$. Thus, we can write

$$\frac{\partial \ell}{\partial \gamma} = \sum_{n=w+1}^N \sum_{m=w+1}^M \left(\frac{\pi y[n,m]^2}{2\mu[n,m]^3} - \frac{2}{\mu[n,m]} \right) \frac{1}{g'(\mu[n,m])} \frac{\partial \eta[n,m]}{\partial \gamma},$$

where

$$\begin{aligned} \frac{\partial \eta[n,m]}{\partial \beta} &= 1 - \sum_{s=0}^q \sum_{t=0}^q \theta_{(s,t)} \frac{\partial \eta[n-s,m-t]}{\partial \beta}, \\ \frac{\partial \eta[n,m]}{\partial \phi_{(i,j)}} &= g(y[n-i,m-j]) - \sum_{s=0}^q \sum_{t=0}^q \theta_{(s,t)} \frac{\partial \eta[n-s,m-t]}{\partial \phi_{(i,j)}}, \\ \frac{\partial \eta[n,m]}{\partial \theta_{(k,l)}} &= g(y[n-k,m-l]) - g(\mu[n-k,m-l]) - \sum_{s=0}^q \sum_{t=0}^q \theta_{(s,t)} \frac{\partial \eta[n-s,m-t]}{\partial \theta_{(k,l)}}, \end{aligned}$$

for $(i,j) \in \{0,1,\dots,p\}^2 - \{(0,0)\}$ and $(l,k) \in \{0,1,\dots,q\}^2 - \{(0,0)\}$.

The Broyden-Fletcher-Goldfarb-Shanno (BFGS) method [Press et al., 1992] with analytic first derivatives was adopted as the nonlinear optimization algorithm [Nocedal and Wright, 1999] to solve (3). The BFGS method was selected due to its superior performance for non-linear optimization [Mittelhammer et al., 2000]. The initial values for the constant (β) and the autoregressive (ϕ) parameters were derived from the ordinary least squares estimate associated to the linear regression model, which has a closed matrix form. The response vector is $(g(y[w+1,w+1]), g(y[w+1,w+2]), \dots, g(y[N,M]))^\top$ and the covariate matrix is given by

$$\begin{bmatrix} 1 & g(y[w,w-1]) & g(y[w-1,w]) & \cdots & g(y[w-p,w-p]) \\ 1 & g(y[w,w]) & g(y[w,w]) & \cdots & g(y[w-p+1,w-p+1]) \\ \vdots & \vdots & \vdots & \ddots & \vdots \\ 1 & g(y[N,M-1]) & g(y[N-1,M]) & \cdots & g(y[N-p,M-p]) \end{bmatrix}.$$

As suggested in Bayer et al. [2020a], we set $\theta = \mathbf{0}$ as initial values.

2.4 Large Data Record Inference

Under some usual regularity conditions, the CMLE is consistent and asymptotically normally distributed [Andersen, 1970]. Thus, in large data records, we have that

$$(\hat{\gamma} - \gamma) \xrightarrow[N \cdot M \rightarrow \infty]{d} \mathbf{N}(\mathbf{0}, \mathbf{I}^{-1}(\gamma)),$$

where \xrightarrow{d} represents convergence in distribution and $\mathbf{N}(\mathbf{0}, \mathbf{I}^{-1}(\gamma))$ denotes the multivariate Gaussian distribution with null mean and covariance matrix $\mathbf{I}^{-1}(\gamma)$. The conditional Fisher information matrix, $\mathbf{I}(\gamma)$, is discussed in detail in the Appendix.

To derive a hypothesis testing methodology tailored for the 2-D RARMA model parameters, the likelihood-based detection theory [Pawitan, 2001, Kay, 1998] can be considered. Let γ be partitioned in a parameter vector of interest γ_I of dimension v , and a vector of nuisance parameters γ_J of dimension $[(p+1)^2 + (q+1)^2 - 1] - v$ [Kay, 1998]. In addi-

tion, $\mathcal{H}_0 : \gamma_I = \gamma_{I_0}$ is the hypothesis of interest and $\mathcal{H}_1 : \gamma_I \neq \gamma_{I_0}$ the alternative hypothesis, where γ_{I_0} is a fixed column vector of dimension v . The Wald statistic is given by [Kay, 1998]

$$T_W = (\hat{\gamma}_{I_1} - \gamma_{I_0})^\top \left(\left[\mathbf{I}^{-1}(\hat{\gamma}_1) \right]_{\gamma_I \gamma_I} \right)^{-1} (\hat{\gamma}_{I_1} - \gamma_{I_0}), \quad (4)$$

where $\hat{\gamma}_1 = (\hat{\gamma}_{I_1}^\top, \hat{\gamma}_{J_1}^\top)^\top$ is the CMLE under \mathcal{H}_1 and $[\mathbf{I}^{-1}(\hat{\gamma}_1)]_{\gamma_I \gamma_I}$ is a partition limited to the estimates of interest of the estimated conditional Fisher information matrix. Under \mathcal{H}_0 , the test statistic, T_W , asymptotically follows the chi-square distribution with v degrees of freedom, χ_v^2 [Kay, 1998]. The hypothesis test consists of comparing the computed value of T_W with a threshold value, ϵ , which is obtained based on the χ_v^2 distribution and the desired probability of false alarm [Kay, 1998].

To test the overall significance of a fitted model, we considered the following hypotheses

$$\begin{cases} \mathcal{H}_0 : \gamma^\star = \mathbf{0}, \\ \mathcal{H}_1 : \gamma^\star \neq \mathbf{0}, \end{cases} \quad (5)$$

where $\gamma^\star = (\phi^\top, \theta^\top)^\top$. Using the Wald test described above, we reject \mathcal{H}_0 when $T_W > \epsilon$. In this situation, $\gamma^\star \neq \mathbf{0}$, indicating that at least some of the autoregressive and moving average parameters are nonzero and the spatial correlation among the pixels is significant.

Additionally, a confidence interval (CI) for the i th component of γ , $i = 1, 2, \dots, (p+1)^2 + (q+1)^2 - 1$, with confidence approximately $100(1 - \alpha)\%$, can be derived based on the CMLE asymptotic distribution as

$$[\hat{\gamma}_i - z_{1-\alpha/2} \text{se}(\hat{\gamma}_i); \hat{\gamma}_i + z_{1-\alpha/2} \text{se}(\hat{\gamma}_i)],$$

where $\text{se}(\hat{\gamma}_i) = \sqrt{\mathbf{I}_{ii}^{-1}(\hat{\gamma})}$ is the standard error (SE) of $\hat{\gamma}_i$, $\mathbf{I}_{ii}^{-1}(\hat{\gamma})$ is the i th element of the diagonal of $\mathbf{I}^{-1}(\hat{\gamma})$, α is the significance level, and z_ρ is the ρ th quantile of the standard normal distribution.

3 Image Modeling and Anomaly Detection

In this section, we propose an image modeling and an anomaly detection tool based on the proposed 2-D RARMA model. We also discuss model selection strategies. For such, we introduce the estimated values of $\mu[n, m]$ and present the residuals of the 2-D RARMA model.

3.1 Image Modeling

The modeled image is obtained by applying the estimated values of $\mu[n, m]$, $\hat{\mu}[n, m]$, in the 2-D RARMA(p, q) model structure, given by (1), and evaluating it at $\hat{\gamma}$. Therefore, the fitted signal is given by

$$\hat{\mu}[n, m] = g^{-1} \left(\hat{\beta} + \sum_{i=0}^p \sum_{j=0}^p \hat{\phi}_{(i,j)} g(y[n-i, m-j]) + \sum_{k=0}^q \sum_{l=0}^q \hat{\theta}_{(k,l)} e[n-k, m-l] \right),$$

where $n = w+1, w+2, \dots, N$ and $m = w+1, w+2, \dots, M$. Hence, similar to the 1-D model, the image border is not included in the modeling process, since the resulting fitted image has $(N-w) \times (M-w)$ pixels.

3.2 Anomaly Detector

Residuals can be useful for performing a diagnostic analysis of the fitted model and can be defined as a function of the observed and predicted values [Kedem and Fokianos, 2005]. We employ the quantile residuals [Dunn and Smyth, 1996],

defined as

$$r[n,m] = \Phi^{-1}(F_Y(y[n,m] | S[n,m])),$$

where Φ^{-1} denotes the standard normal quantile function. When the model is correctly fitted, for construction, the quantile residuals are approximately Gaussian distributed with zero mean and unit variance, i.e., $r[n,m] \sim \mathcal{N}(0,1)$ [Dunn and Smyth, 1996]. The residual analysis for other classes of 1-D non-Gaussian dynamical models is discussed in Kedem and Fokianos [2005] and Dunn and Smyth [1996].

Large values of $r[n,m]$ can be interpreted as anomaly changes in the image behavior. To capture such variations of the residual values, we adopted the use of control charts. Since the residuals have approximately unitary variance, the control chart detects an image change if the residual value is outside the control limit $\pm L$. We adopted $L = 3$, since it is expected that residuals are randomly distributed around zero and inside the interval $[-3,3]$, about 99.7% of the observations, since $2\Phi(L) - 1|_{L=3} \approx 99.7\%$ [Brooks et al., 2013, Bayer et al., 2019]. If the residual value is outside this range, the analyzed pixel is understood to differ from the expected behavior according to the 2-D RARMA model fitted in the region of interest and, consequently, some anomaly change might have occurred.

Notice that the proposed model relies on neighboring pixels from the northwest direction, as shown in Figure 1. Thus, to take into account the other directions in an omnidirectional manner, thus ensuring that all surrounding pixels are considered, the 2-D RARMA fitting is also applied to the 90° , 180° , and 270° rotated region of interest to capture information from the versions of the southwest, southeast, and northeast directions. Results are combined according to the morphological union of the resulting binary images. Search for the best model for each rotation is computationally expensive. Consequently, considering a trade-off between simplicity and efficacy of the anomaly detection method, we suggest using the same model order for the four directions.

To further increase the performance of the proposed detector, a post-processing step using mathematical morphological operations, such as erosion, dilation, opening, and closing operations, can be considered [Edmond et al., 2000, Gonzalez et al., 2009]. Such operations aim at (i) removing small spurious pixel groups which are regarded as noise and (ii) preventing the splitting of the interest targets into multiple substructures [Gonzalez et al., 2009]. The resulting data is the detected image. The proposed ground type change detection method is summarized in Algorithm 1.

Algorithm 1 Anomaly detection method based on the 2-D RARMA(p,q) model

Require: Interest image $\mathbf{X}_{\text{input}}$

Ensure: Anomaly detection image $\mathbf{X}_{\text{detected}}$

1) Select region of interest $\mathbf{X}_{\text{selected}} \subset \mathbf{X}_{\text{input}}$ which anomaly detection is to be tested against.

2) Fit the 2-D RARMA(p,q) model for the following images:

$\mathbf{X}_0 = \mathbf{X}_{\text{selected}}$

$\mathbf{X}_k = \text{rot90}(\mathbf{X}_{k-1})$,

for $k = 1, 2, 3$, where $\text{rot90}(\cdot)$ rotates its argument counterclockwise by 90 degrees.

3) For each resulting fitted image, compute residuals $r_k[n,m]$ relative to $\mathbf{X}_{\text{input}}$.

4) Obtain four binary images as follows

if $(r_k[n,m] \leq -3)$ or $(r_k[n,m] \geq 3)$ **then**

$\tilde{X}_k[n,m] \leftarrow 1$

else

$\tilde{X}_k[n,m] \leftarrow 0$

end if

for $k = 0, 1, 2, 3$.

5) Compute binary image from the following pixel-wise Boolean union: $\tilde{\mathbf{X}} \leftarrow \bigcup_{k=0}^3 \tilde{X}_k$.

6) Apply morphological operators as a final post-processing step: $\mathbf{X}_{\text{detected}} \leftarrow \text{post-processing}(\tilde{\mathbf{X}})$.

3.3 Model Selection

To perform the model selection, we considered the three-stage iterative Box-Jenkins methodology [Box et al., 2008], which is based on the following steps: identification, estimation, and statistical model checking. For the first step, we suggest to use the Akaike's (AIC) [Akaike, 1974] and Schwartz's (SIC) [Schwarz et al., 1978] information criteria to define some rough boundaries on the choice of p and q orders. The AIC and SIC are given by

$$\begin{aligned} \text{AIC} &= -2\ell(\hat{\gamma}) + 2\kappa, \\ \text{SIC} &= -2\ell(\hat{\gamma}) + \kappa \log(N \times M), \end{aligned}$$

where $\kappa = (p+1)^2 + (q+1)^2 - 1$ is the number of estimated parameters in the fitted model. Lower AIC and SIC values are related to more suitable models. The estimation step is done by the conditional maximum likelihood method, as explored in Section 2.3.

Regarding the model checking step, we suggest to consider the following approach: (i) test the overall significance of the fitted model through the Wald test introduced in Section 2.4; (ii) perform graphic analysis to check whether the model residuals are randomly distributed around zero; and (iii) compute the mean square error (MSE) and the mean absolute percentage error (MAPE) between $y[n, m]$ and $\hat{\mu}[n, m]$ among the candidate fitted models. Lower MSE and MAPE values are specially desired in detection problems because good quality predictions imply in accurate detection results. As well as in the Box-Jenkins method, if the fitted model is not suitable according to any of the steps described above, then we have to return to the first step and attempt to build a better model.

4 Numerical Results

In this section, we aim at evaluating the CMLE of the 2-D RARMA model parameters and assessing the performance of the proposed image modeling and anomaly detector. For such, the proposed analyses were performed in the context of SAR image processing. We performed three numerical experiments: (i) a simulated data analysis to assess the proposed estimators and (ii) two computations aiming at anomaly detection based on actual SAR images.

4.1 Analysis with Simulated Data

Rayleigh distributed data $y[n, m]$ were generated by the inversion method with mean given by (1) and logarithm link function. We considered simulations under two scenarios: (i) 2-D RARMA(1,0) model and (ii) 2-D RARMA(1,1) model. The parameter values were selected based on estimated values of the 2-D RARMA model parameters from a SAR image forest region acquired by the airborne CARABAS II system [Lundberg et al., 2006], a Swedish ultrawideband (UWB) very-high frequency (VHF) SAR device operating at horizontal (HH) polarization. Details related to the data can be found in Ulander et al. [2005] and Lundberg et al. [2006]. The obtained numerical values of the parameters were $\beta = -0.2031$, $\phi_{(0,1)} = 0.4562$, $\phi_{(1,0)} = 0.4523$, and $\phi_{(1,1)} = -0.1054$, for the 2-D RARMA(1,0) model; and $\beta = 0.3569$, $\phi_{(0,1)} = 0.2155$, $\phi_{(1,0)} = 0.2032$, $\phi_{(1,1)} = 0.1500$, $\theta_{(0,1)} = 0.1529$, $\theta_{(1,0)} = 0.1744$, and $\theta_{(1,1)} = 0.1998$, for the 2-D RARMA(1,1) model. The number of Monte Carlo replications was set to 1,000 and the sizes of the synthetic images were $\{10 \times 10, 20 \times 20, 40 \times 40, 80 \times 80\}$.

In order to numerically evaluate the point estimators, we computed the mean, percentage relative bias (RB%), and mean square error (MSE) of the CMLE. A graphical analysis of the point estimators is performed through graphs of total relative bias and total mean square error. Both measures are defined as the sum of the absolute values of the individual relative biases and mean square error and are displayed in Figures 2(a) and 2(b), respectively.

Tables 1 and 2 present the simulation results for 2-D RARMA(1,0) and 2-D RARMA(1,1) models, respectively. As expected, both bias and MSE figures improve when larger images are considered. This behavior is in agreement with the asymptotic property (consistency) of the CMLE. Convergence failures were absent for all considered scenarios. In contrast

Table 1: Simulation results on point and interval estimation of the 2-D RARMA(1,0) model

Measures	Mean	RB(%)	MSE	CR
$N = M = 10$				
$\hat{\beta}$	-0.2629	29.4370	0.0244	0.9230
$\hat{\phi}_{(0,1)}$	0.4385	-3.8767	0.0071	0.9400
$\hat{\phi}_{(1,0)}$	0.4339	-4.0692	0.0073	0.9360
$\hat{\phi}_{(1,1)}$	-0.0998	-5.2979	0.0081	0.9430
$N = M = 20$				
$\hat{\beta}$	-0.2160	6.3468	0.0051	0.9360
$\hat{\phi}_{(0,1)}$	0.4523	-0.8514	0.0014	0.9400
$\hat{\phi}_{(1,0)}$	0.4492	-0.6841	0.0014	0.9510
$\hat{\phi}_{(1,1)}$	-0.1054	-0.0223	0.0016	0.9600
$N = M = 40$				
$\hat{\beta}$	-0.2063	1.5865	0.0012	0.9520
$\hat{\phi}_{(0,1)}$	0.4551	-0.2409	0.0003	0.9550
$\hat{\phi}_{(1,0)}$	0.4514	-0.2021	0.0003	0.9440
$\hat{\phi}_{(1,1)}$	-0.1049	-0.4706	0.0004	0.9520
$N = M = 80$				
$\hat{\beta}$	-0.2043	0.6020	0.0003	0.9520
$\hat{\phi}_{(0,1)}$	0.4560	-0.0464	0.0001	0.9430
$\hat{\phi}_{(1,0)}$	0.4516	-0.1504	0.0001	0.9520
$\hat{\phi}_{(1,1)}$	-0.1052	-0.1450	0.0001	0.9640

to the traditional 2-D ARMA model, the proposed model avoids the estimation problem of the MA parameters, as discussed in Kizilkaya and Kayran [2005] and Lim [1990]. The derived model estimates the AR and MA terms simultaneously; and $\hat{\phi}$ and $\hat{\theta}$ present closer values of RB(%) for all considered synthetic images. The image size of 40×40 was sufficiently large for accurate inference in 2-D RARMA(1,0) model, i.e., MSE and RB(%) values close to zero. On the other hand, the 2-D RARMA(1,1) model shows accurate inference results for an image size of 80×80 pixels. We can verify graphically from Figures 2(a) and 2(b) that the RB% and the MSE decrease as the image size increases in both evaluated models, numerically indicating the estimator consistency.

To evaluate the interval estimators, we computed the coverage rate (CR) of the confidence intervals with a significance level of 5%. The CR is defined according the following steps: (i) in each Monte Carlo replication, compute the CI and interrogate whether the CI contains the true parameter or not and (ii) define the percentage of replications for which the parameter is in the CI. It is desirable that the CR approaches the nominal coverage level $100(1 - \alpha)\%$. The CR values in Tables 1 and 2 are close to the nominal value of 0.95 in all considered scenarios, specially for larger image sizes.

4.2 Analysis with Real Data

In this section, we perform two anomaly detection experiments considering two different amplitude SAR images. For that, we use the methodology proposed in Section 3.2. We do not have access to the complex data of the tested SAR images, and consequently, it is not possible to check if the real and complex parts approaches the Gaussian distribution with zero mean and constant variance, as discussed in [Kuruoglu and Zerubia, 2004, Yue et al., 2021]. However, evidence of the usefulness of the Rayleigh distribution for describing image pixel amplitude values is found in Kuruoglu and Zerubia [2004], Yue et al. [2021]. Moreover, the results obtained in this paper suggest that the 2-D RARMA model provides good anomaly detection and modeling for SAR data.

Table 2: Simulation results on point and interval estimation of the 2-D RARMA(1,1) model

Measures	Mean	RB(%)	MSE	CR
$N = M = 10$				
$\hat{\beta}$	0.2834	-20.5927	0.0223	0.7960
$\hat{\phi}_{(0,1)}$	0.2278	5.7302	0.0405	0.8400
$\hat{\phi}_{(1,0)}$	0.2266	11.5074	0.0388	0.8180
$\hat{\phi}_{(1,1)}$	0.1758	17.1830	0.0483	0.7680
$\hat{\theta}_{(0,1)}$	0.1371	-10.3477	0.0583	0.8100
$\hat{\theta}_{(1,0)}$	0.1413	-18.9945	0.0604	0.8060
$\hat{\theta}_{(1,1)}$	0.1582	-20.8355	0.0493	0.8350
$N = M = 20$				
$\hat{\beta}$	0.3312	-7.2026	0.0036	0.9060
$\hat{\phi}_{(0,1)}$	0.2246	4.2177	0.0078	0.9140
$\hat{\phi}_{(1,0)}$	0.2124	4.5210	0.0081	0.9120
$\hat{\phi}_{(1,1)}$	0.1689	12.6150	0.0095	0.8890
$\hat{\theta}_{(0,1)}$	0.1428	-6.5797	0.0090	0.9190
$\hat{\theta}_{(1,0)}$	0.1673	-4.0788	0.0089	0.9120
$\hat{\theta}_{(1,1)}$	0.1753	-12.2650	0.0061	0.9200
$N = M = 40$				
$\hat{\beta}$	0.3456	-3.1658	0.0009	0.9200
$\hat{\phi}_{(0,1)}$	0.2195	1.8514	0.0018	0.9400
$\hat{\phi}_{(1,0)}$	0.2077	2.2177	0.0019	0.9290
$\hat{\phi}_{(1,1)}$	0.1610	7.3560	0.0023	0.9150
$\hat{\theta}_{(0,1)}$	0.1499	-1.9723	0.0020	0.9390
$\hat{\theta}_{(1,0)}$	0.1711	-1.9205	0.0020	0.9310
$\hat{\theta}_{(1,1)}$	0.1878	-5.9962	0.0013	0.9280
$N = M = 80$				
$\hat{\beta}$	0.3514	-1.5381	0.0002	0.9100
$\hat{\phi}_{(0,1)}$	0.2184	1.3555	0.0005	0.9290
$\hat{\phi}_{(1,0)}$	0.2059	1.3082	0.0005	0.9400
$\hat{\phi}_{(1,1)}$	0.1549	3.2791	0.0006	0.9360
$\hat{\theta}_{(0,1)}$	0.1503	-1.7221	0.0005	0.9420
$\hat{\theta}_{(1,0)}$	0.1717	-1.5643	0.0005	0.9330
$\hat{\theta}_{(1,1)}$	0.1932	-3.3146	0.0003	0.9350

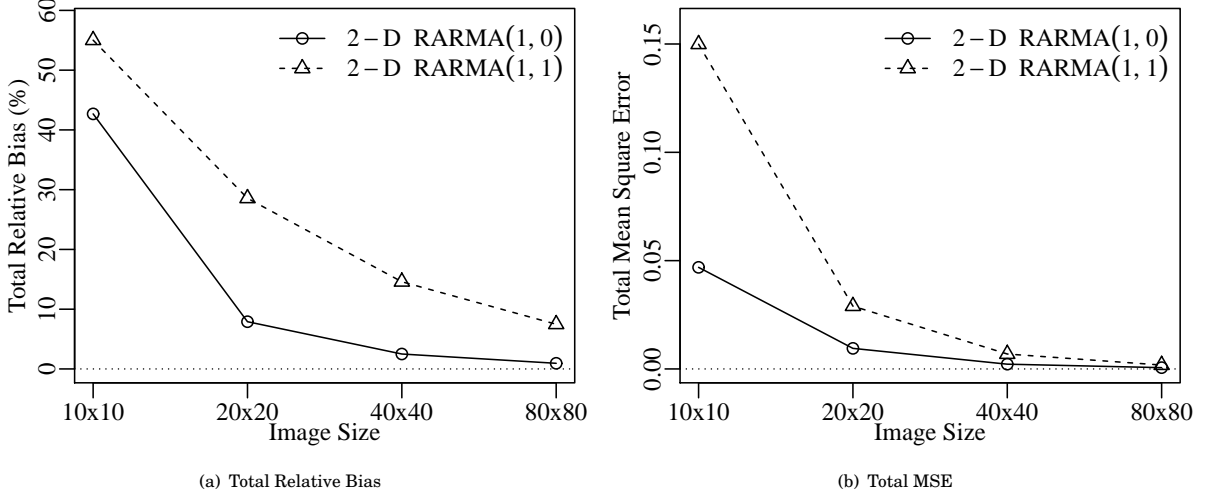


Figure 2: Total relative bias and mean square error of the 2-D RARMA(1,0) and 2-D RARMA(1,1) model estimators.

4.2.1 CARABAS II

The SAR image considered in this experiment was collected by the CARABAS II system described in the previous subsection. As reported in Ulander et al. [2005], the spatial resolution of CARABAS II is about 3 m in azimuth and range. The ground scene of the selected image is dominated by pine forest, a lake, and 25 military vehicles [Lundberg et al., 2006]. The forest and lake regions characterize most of the image area and they follow a homogeneous pattern. The military vehicles deployed in the SAR scene [Lundberg et al., 2006] introduce more representative behavior changing when compared to the forest and lake regions. For instance, the sample mean value of forest, lake and military vehicles areas are about 0.1267, 0.1148, and 0.2863, respectively, i.e., the sample mean value of military vehicles region is roughly three times the forest and lake regions. Pixels related to power line areas show similar amplitude values with the targets, and consequently, are strongly associated to the false alarm detection, as discussed in Lundberg et al. [2006]. The considered SAR image in this experiment is shown in Figure 3.

The model selection was based on the steps described in Section 3.3. We employed the search space restricted to models with $(p, q) \in \{0, 1, 2\}$ and the size of the considered region of interest was $N = M \in \{10, 20, 40, 80\}$. As a result, we obtained the following optimal parameters: (i) $p = q = 1$ and (ii) $N = M = 80$. The selected region of interest in this section was forest. For the post-processing step, we followed the methodology defined in Lundberg et al. [2006], where we considered two morphology operations, namely, an opening operation followed by a dilation. The opening uses a 3×3 pixels square structuring element, whose size is determined by the system resolution; the dilation considers a 7×7 pixels structuring element, which is linked to the approximate size of the military vehicles. Table 3 shows the estimated parameters and standard error (SE) for each rotated image, as described in the second step of the Algorithm 1. The overall significance Wald test p -value can be found in Table 3, showing that the spatial autocorrelation is significant for a probability of false alarm equal to 0.05. Figure 4 shows the residual versus index charts of the 2-D RARMA(1,1) models. As expected, the residuals are randomly distributed and present values close to zero.

For comparison purposes, we also obtained the detection results based on the 2-D ARMA(1,1) model. Detection results for both 2-D RARMA(1,1) and 2-D ARMA(1,1) models can be found in Figures 5(a) and 5(b), respectively. For a better visualization, Figure 5 shows the zoomed images in the region where ground type changes were detected. The proposed method detected 24 military vehicles and five false alarms. In contrast, the 2-D ARMA(1,1) model can only detect 16 military vehicles and two false alarms.

We also compared the proposed methodology with three different competing approaches: (i) constant false alarm rate

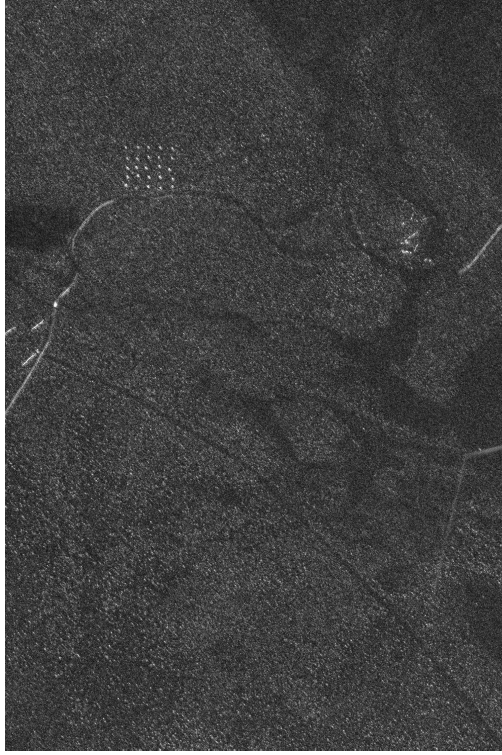


Figure 3: Original CARABAS II SAR image.

Table 3: Estimated parameters, standard error (SE), and p -values of the overall significance Wald test of the 2-D RARMA(1,1) model for the CARABAS II SAR image

	Rotated Image							
	Northwest		Southwest		Southeast		Northeast	
	Estimate	SE	Estimate	SE	Estimate	SE	Estimate	SE
$\hat{\beta}$	-1.2274	0.0681	-1.1146	0.0854	-1.1986	0.0666	-1.2076	0.0892
$\hat{\phi}_{(0,1)}$	0.1723	0.0303	0.1659	0.0396	0.2218	0.0308	0.1912	0.0392
$\hat{\phi}_{(1,0)}$	0.1526	0.0316	0.2206	0.0351	0.1572	0.0316	0.1616	0.0361
$\hat{\phi}_{(1,1)}$	0.0675	0.0303	0.0512	0.0275	0.0294	0.0308	0.0387	0.0270
$\hat{\theta}_{(0,1)}$	0.1773	0.0329	0.1263	0.0418	0.1305	0.0336	0.1127	0.0416
$\hat{\theta}_{(1,0)}$	0.1646	0.0338	0.1208	0.0378	0.1808	0.0335	0.1685	0.0383
$\hat{\theta}_{(1,1)}$	0.1935	0.0252	-0.0691	0.0250	0.2064	0.0251	-0.0461	0.0256
p -value	< 0.001		< 0.001		< 0.001		< 0.001	

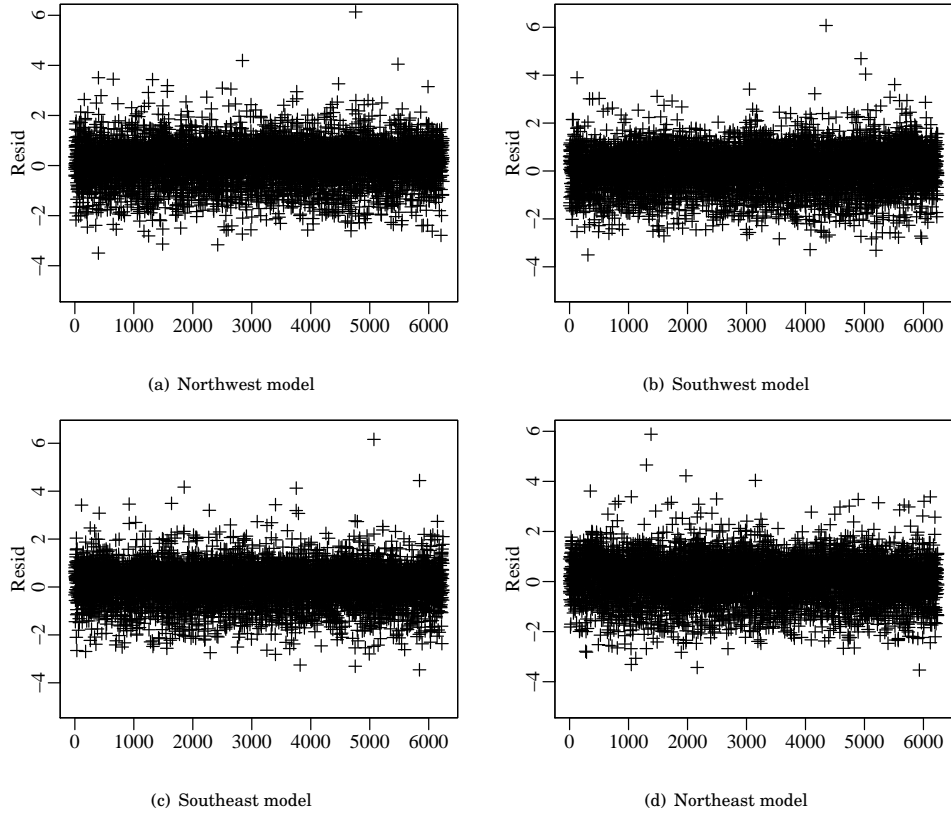


Figure 4: Residual charts of the 2-D RARMA(1,1) models for the CARABAS II SAR image.

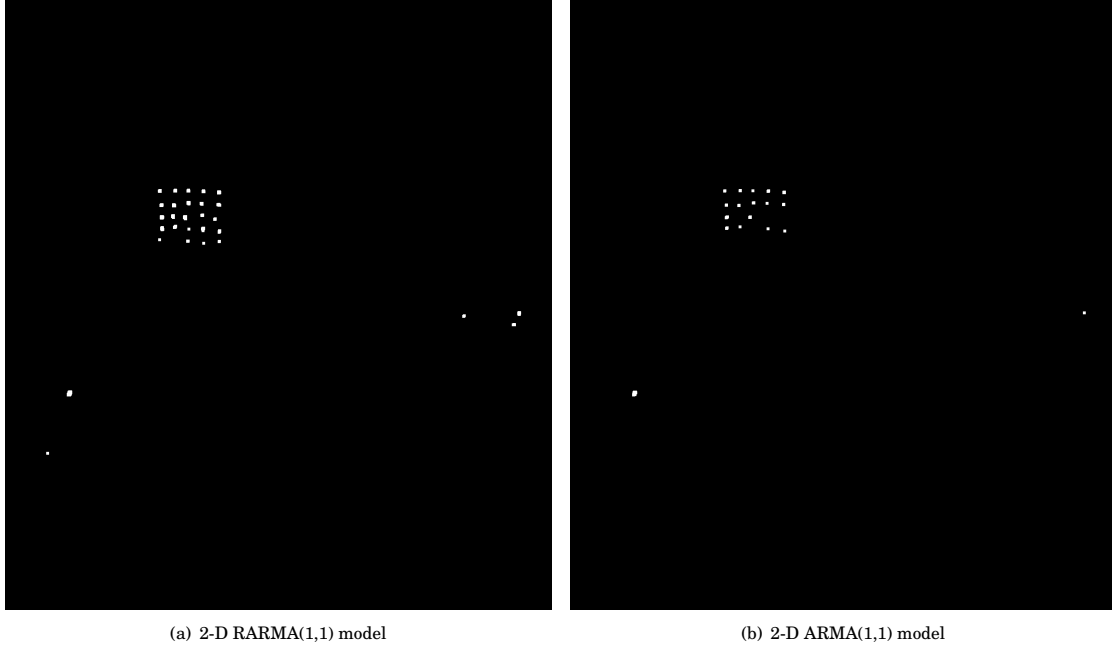


Figure 5: Zoomed detected images in the region where anomaly changes were identified, considering 2-D RARMA(1,1) and 2-D ARMA(1,1) models.

Table 4: Measures of quality of the fitted CARABAS II SAR image based on 2-D RARMA(1,1) and 2-D ARMA(1,1) models

	Model	
	2-D RARMA(1,1)	2-D ARMA(1,1)
MSE	0.0562	0.1241
MAPE	0.4277	0.7499

filtering combined with likelihood ratio test assuming the Gaussian distribution [Lundberg et al., 2006], (ii) a statistical hypothesis test for wavelength-resolution incoherent SAR ground type change detection based on the bivariate gamma distribution [Vu et al., 2018]; and (iii) a statistical hypothesis test considering the bivariate Gaussian distribution [Vu, 2017]. Differently from the above methods, our detection scheme requires only one input image for analysis; whereas two images are demanded in Lundberg et al. [2006] and Vu et al. [2018], respectively, and three in Vu [2017]. Despite requiring much less assumptions and data information (only one image scene look vs several image scene looks) when compared to Lundberg et al. [2006], Vu et al. [2018], and Vu [2017], the proposed 2-D RARMA(1,1) model performance was very close to the competing methods: only one less detection hit; and 3 to 5 more false alarms.

To further compare the image modeling performance of the evaluated models, we computed the MSE and MAPE of all pixels. Table 4 summarizes the results of the quality adjustment measures for 2-D RARMA(1,1) and 2-D ARMA(1,1) models. The 2-D RARMA(1,1) model excels in terms of MSE and MAPE measures. The execution time of this experiment considering the Rayleigh- and Gaussian-based models were 90.24 and 11.43 seconds, respectively. The elapsed time of the 2-D RARMA model is higher than the Gaussian model, as also observed in other type of non-Gaussian models which require iterative optimization method for estimation.



Figure 6: Original San Francisco SAR image HH associated polarization channel.

4.2.2 San Francisco Bay

The considered SAR image in this section is the San Francisco Bay, obtained by the AIRSAR sensor at band L with four looks [Cintra et al., 2013]. As reported in Safaei and Sahebi [2019], the San Francisco Bay image is multilooked by a factor of approximately 10 m in azimuth and range. Figure 6 shows the amplitude data of the 200×350 San Francisco Bay image associated to the HH polarization channel. The ground scene of the evaluated image is dominated by ocean (dark ground—top and left part of the image), forest (gray ground), and urban area (light ground—bottom) [Nascimento et al., 2013].

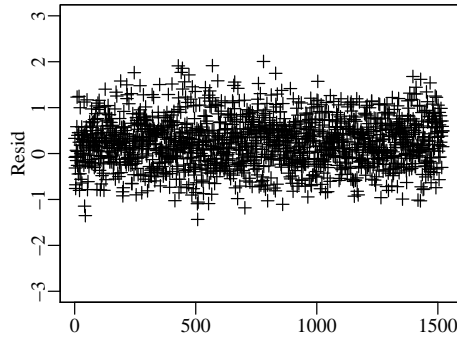
To perform the ground type change detection in the San Francisco SAR image, we set the following parameters in Algorithm 1 adopting the same methodology described in the previous subsection. As discussed in Yue et al. [2019], each statistical model is suitable for one type of specific scenario of terrain surface. In particular, the Rayleigh distribution is adequate to represent homogeneous areas [Oliver and Quegan, 2004], such as pasture, crops, and sea ground type [Cintra et al., 2013]; consequently, the region of interest in this section is linked to the ocean area. Hence, non-ocean regions (forest and urban areas) are expected to trigger a detection, suggesting an anomaly change. Considering the methodology described in Section 3.3, we have that (i) $p = 1$ and $q = 0$; and (ii) $N = M = 40$. In the post-processing step, we considered two mathematical morphology steps, namely, closing and opening operations. The dilation considered in both steps used a 10×10 pixels square structuring element, whose size is determined by the system resolution and the size of the evaluated areas.

Because $q = 0$, we have that $\theta = \mathbf{0}$, and therefore, $\gamma^* = (\phi^\top, \mathbf{0}^\top)^\top$ in (5). The estimated parameters and SE for each rotated image, as described in the second step of the Algorithm 1, are shown in Table 5. The p -values of the Wald test are also reported in Table 5, indicating that the spatial autocorrelation is significant for a probability of false alarm equal to 0.05. Regarding the diagnostic analysis of the fitted model, as displayed in Figure 7, the model residuals are randomly distributed and present values close to zero.

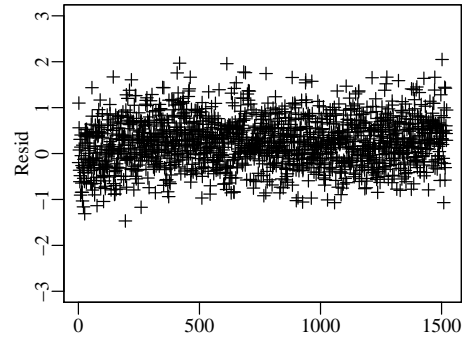
The anomaly detection results can be found in Figure 8. Detection results were compared to the ones based on the 2-D ARMA(1,0). The results for the detectors considering the 2-D RARMA and 2-D ARMA can be found in Figures 8(a) and 8(b), respectively. Both evaluated detectors identified the difference among the ocean ground type from the urban and forest areas in the tested SAR image. We also compared the proposed methodology with the ones presented in Gomez et al. [2017], where machine learning optimization strategies were used as classification techniques. With a visual inspection, our model and Gomez et al. [2017] equally well classified the ocean ground type. Finally, we computed the MSE and MAPE figures of merit to evaluate the fitted image. The 2-D RARMA(1,0) model outperforms the alternative model in term of

Table 5: Estimated parameters, standard error (SE), and p -values of the overall significance Wald test of the 2-D RARMA(1,0) model for the San Francisco SAR image

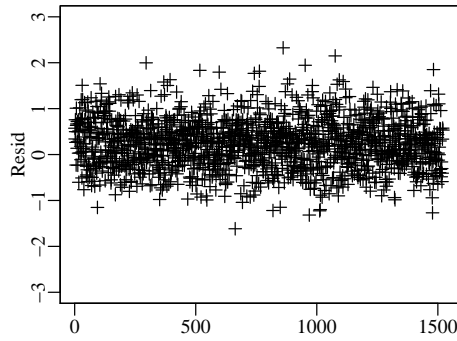
	Rotated Image							
	Northwest		Southwest		Southeast		Northeast	
	Estimate	SE	Estimate	SE	Estimate	SE	Estimate	SE
$\hat{\beta}$	-1.2078	0.1378	-1.1879	0.1391	-1.2109	0.1485	-1.1095	0.14834
$\hat{\phi}_{(0,1)}$	0.1408	0.0440	0.4388	0.0387	0.1516	0.0432	0.4350	0.0404
$\hat{\phi}_{(1,0)}$	0.4412	0.0389	0.1236	0.0439	0.4389	0.0404	0.1608	0.0431
$\hat{\phi}_{(1,1)}$	-0.0023	0.0438	0.0247	0.0438	-0.0071	0.0452	0.0238	0.0452
p -value	< 0.001		< 0.001		< 0.001		< 0.001	



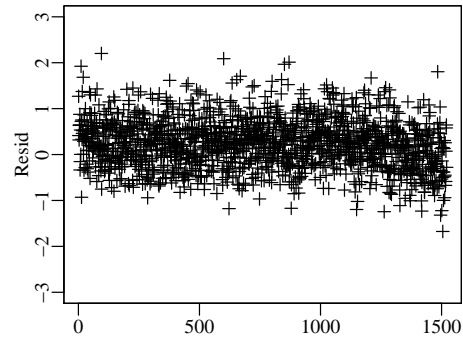
(a) Northwest model



(b) Southwest model



(c) Southeast model



(d) Northeast model

Figure 7: Residual charts of the 2-D RARMA(1,0) models for the San Francisco SAR image.

Table 6: Measures of quality of the fitted San Francisco SAR image based on 2-D RARMA(1,0) and 2-D ARMA(1,0) models

	Model	
	2-D RARMA(1,0)	2-D ARMA(1,0)
MSE	0.2255	0.3191
MAPE	0.3405	0.9711



Figure 8: Detected images associated to the HH polarization channel based on the 2-D RARMA(1,0) and 2-D ARMA(1,0) models.

MSE and MAPE measures, as can be verified in Table 6. The elapsed time execution for the 2-D RARMA model was equal to 3.29 seconds, while for the Gaussian-based model, we had an elapsed time of 2.76 seconds, i.e., difference between both models is less than one second in this experiment.

5 Conclusions

In this paper, we proposed the 2-D RARMA model for SAR image modeling. We introduced an inference approach for the model parameters, the conditional Fisher information matrix, and the asymptotic properties of the CMLE. Monte Carlo simulations were used to evaluate the performance of the CMLE. The proposed model was applied for modeling and anomaly detection in SAR images, showing competitive results when compared to 2-D ARMA models. Moreover, although the proposed approach requires much less information when compared to Lundberg et al. [2006], Vu et al. [2018], and Vu [2017], it offered detection results very close to the figures reported in Lundberg et al. [2006], Vu et al. [2018], and Vu [2017] for the CARABAS II SAR image and in Gomez et al. [2017], for the San Francisco image. The proposed model is presented as a suitable tool for image modeling and anomaly detection in the context of Rayleigh distributed data, in general, and SAR image processing, in particular.

Acknowledgement

This work was supported in part by Conselho Nacional de Desenvolvimento Científico e Tecnológico (CNPq), Coordenação de Aperfeiçoamento de Pessoal de Nível Superior (CAPES), Fundação de Amparo à Pesquisa do Estado do Rio Grande do Sul (FAPERGS), Brazil; and Swedish-Brazilian Research and Innovation Centre (CISB), and Saab AB, Sweden.

A Conditional Fisher Information Matrix

In this Appendix, we provide the conditional Fisher information matrix, which is given by the expectation of the negative value of the second-order partial derivatives of the log-likelihood function, which is defined as follows

$$\begin{aligned} \frac{\partial^2 \ell(\gamma)}{\partial \gamma_i \partial \gamma_j} &= \sum_{n=1}^N \sum_{m=1}^M \frac{d}{d\mu[n,m]} \left(\frac{d\ell[n,m](\mu[n,m])}{d\mu[n,m]} \frac{d\mu[n,m]}{d\eta[n,m]} \right) \frac{d\mu[n,m]}{d\eta[n,m]} \frac{\partial \eta[n,m]}{\partial \gamma_j} \frac{\partial \eta[n,m]}{\partial \gamma_i} \\ &= \sum_{n=1}^N \sum_{m=1}^M \left(\frac{\partial^2 \ell[n,m](\mu[n,m])}{\partial \mu[n,m]^2} \frac{d\mu[n,m]}{d\eta[n,m]} + \frac{d\ell[n,m](\mu[n,m])}{d\mu[n,m]} \frac{\partial}{\partial \mu[n,m]} \frac{d\mu[n,m]}{d\eta[n,m]} \right) \\ &\quad \cdot \frac{d\mu[n,m]}{d\eta[n,m]} \frac{\partial \eta[n,m]}{\partial \gamma_j} \frac{\partial \eta[n,m]}{\partial \gamma_i}. \end{aligned}$$

As shown in Palm et al. [2019], we have that $E(d\ell[n,m](\mu[n,m])/d\mu[n,m] | S[n,m]) = 0$. Thus,

$$E \left(\frac{\partial^2 \ell(\gamma)}{\partial \gamma_i \partial \gamma_j} \middle| S[n,m] \right) = \sum_{n=1}^N \sum_{m=1}^M E \left(\frac{\partial^2 \ell[n,m](\mu[n,m])}{\partial \mu[n,m]^2} \right) \left(\frac{d\mu[n,m]}{d\eta[n,m]} \right)^2 \frac{\partial \eta[n,m]}{\partial \gamma_j} \frac{\partial \eta[n,m]}{\partial \gamma_i}.$$

The derivatives of $d\ell[n,m](\mu[n,m])/d\mu[n,m]$, $d\mu[n,m]/d\eta[n,m]$, and $\partial \eta[n,m]/\partial \gamma$ have been defined in Section 2.3. Now, the second derivative of $d\ell[n,m](\mu[n,m])/d\mu[n,m]$ is given by

$$\frac{\partial^2 \ell[n,m](\mu[n,m])}{\partial \mu[n,m]^2} = \frac{2}{\mu[n,m]^2} - \frac{3\pi y[n,m]^2}{2\mu[n,m]^4}.$$

Taking the expected value, we have $E \left[\frac{d^2 \ell[n,m](\mu[n,m])}{d\mu[n,m]^2} \right] = -\frac{4}{\mu[n,m]^2}$. Thus,

$$E \left[\frac{\partial^2 \ell(\gamma)}{\partial \gamma_i \partial \gamma_j} \right] = \sum_{n=1}^N \sum_{m=1}^M -\frac{4}{\mu[n,m]^2} \left(\frac{1}{g'(\mu[n,m])} \right)^2 \frac{\partial \eta[n,m]}{\partial \gamma_j} \frac{\partial \eta[n,m]}{\partial \gamma_i}.$$

The conditional Fisher information matrix is given by

$$\mathbf{I}(\gamma) = - \begin{bmatrix} I_{(\beta,\beta)} & \mathbf{I}_{(\beta,\phi)} & \mathbf{I}_{(\beta,\theta)} \\ \mathbf{I}_{(\phi,\beta)} & \mathbf{I}_{(\phi,\phi)} & \mathbf{I}_{(\phi,\theta)} \\ \mathbf{I}_{(\theta,\beta)} & \mathbf{I}_{(\theta,\phi)} & \mathbf{I}_{(\theta,\theta)} \end{bmatrix},$$

where $I_{(\beta,\beta)} = \mathbf{a}^\top \mathbf{W} \mathbf{a}$, $\mathbf{I}_{(\beta,\phi)} = \mathbf{P}^\top \mathbf{W} \mathbf{a}$, $\mathbf{I}_{(\beta,\theta)} = \mathbf{R}^\top \mathbf{W} \mathbf{a}$, $\mathbf{I}_{(\phi,\beta)} = \mathbf{a}^\top \mathbf{W} \mathbf{P}$, $\mathbf{I}_{(\phi,\phi)} = \mathbf{P}^\top \mathbf{W} \mathbf{P}$, $\mathbf{I}_{(\phi,\theta)} = \mathbf{R}^\top \mathbf{W} \mathbf{P}$, $\mathbf{I}_{(\theta,\alpha)} = \mathbf{a}^\top \mathbf{W} \mathbf{R}$, $\mathbf{I}_{(\theta,\phi)} = \mathbf{P}^\top \mathbf{W} \mathbf{R}$, $\mathbf{I}_{(\theta,\theta)} = \mathbf{R}^\top \mathbf{W} \mathbf{R}$. The matrices \mathbf{P} and \mathbf{R} are of dimensions $(N \cdot M - w) \times (p+1)^2 - 1$, and $(N \cdot M - w) \times (q+1)^2 - 1$, respectively, with (i,j) th element given by $\mathbf{P}[i,j] = \frac{\partial \eta[i+w,j+w]}{\partial \phi_{(i,j)}}$ and $\mathbf{R}[i,j] = \frac{\partial \eta[i+w,j+w]}{\partial \theta_{(i,j)}}$. Finally, we have that

$$\mathbf{W} = \text{diag} \left\{ \frac{4}{\mu[1,1]^2} \left(\frac{d\mu[1,1]}{d\eta[1,1]} \right)^2, \frac{4}{\mu[1,2]^2} \left(\frac{d\mu[1,2]}{d\eta[1,2]} \right)^2, \dots, \frac{4}{\mu[N,M]^2} \left(\frac{d\mu[N,M]}{d\eta[N,M]} \right)^2 \right\},$$

and $\mathbf{a} = \left(\frac{\partial \eta[n+1,m+1]}{\partial \beta}, \frac{\partial \eta[n+2,m+2]}{\partial \beta}, \dots, \frac{\partial \eta[N,M]}{\partial \beta} \right)^\top$.

References

- Oscar Bustos, Silvia Ojeda, and Ronny Vallejos. Spatial ARMA models and its applications to image filtering. *Brazilian Journal of Probability and Statistics*, 23(2):141–165, 2009a.
- Aydin Kizilkaya and A H Kayran. ARMA-cepstrum recursion algorithm for the estimation of the MA parameters of 2-D ARMA models. *Multidimensional Systems and Signal Processing*, 16(4):397–415, 2005.
- Silvia Ojeda, Ronny Vallejos, and Oscar Bustos. A new image segmentation algorithm with applications to image inpainting. *Computational Statistics & Data Analysis*, 54(9):2082–2093, 2010.

- Oscar H Bustos, Marcelo Ruiz, Silvia Ojeda, Ronny Vallejos, and Alejandro C Frery. Asymptotic behavior of RA-estimates in autoregressive 2D processes. *Journal of Statistical Planning and Inference*, 139(10):3649–3664, 2009b.
- Azriel Rosenfeld. *Image modeling*. Academic Press, New York, USA, 2014.
- Yousef W Nijim, Samuel D Stearns, and Wasfy B Mikhael. Lossless compression of images employing a linear IIR model. In *IEEE International Symposium on Circuits and Systems*, volume 2, pages 305–308, 1996.
- Y-S Chung and Morton Kanefsky. On 2-D recursive LMS algorithms using ARMA prediction for ADPCM encoding of images. *IEEE Transactions on Image Processing*, 1(3):416–422, 1992.
- Jae S Lim. *Two-dimensional signal and image processing*. Prentice Hall, New Jersey, USA, 1990.
- Ronny O Vallejos and Tomislav J Mardesic. A recursive algorithm to restore images based on robust estimation of NSHP autoregressive models. *Journal of Computational and Graphical Statistics*, 13(3):674–682, 2004.
- Peter J Brockwell and Richard A Davis. *Introduction to time series and forecasting*. Springer, Switzerland, 2016.
- Thomas E Hall and Georgios B Giannakis. Bispectral analysis and model validation of texture images. *IEEE Transactions on Image Processing*, 4(7):996–1009, 1995.
- Rangasami L Kashyap and K-B Eom. Robust image modeling techniques with an image restoration application. *IEEE Transactions on Acoustics, Speech, and Signal Processing*, 36(8):1313–1325, 1988.
- Jesse Bennett and Alireza Khotanzad. Maximum likelihood estimation methods for multispectral random field image models. *IEEE Transactions on Pattern Analysis and Machine Intelligence*, 21(6):537–543, 1999.
- Sabyasachi Basu and Gregory C Reinsel. Properties of the spatial unilateral first-order ARMA model. *Advances in Applied Probability*, 25(3):631–648, 1993.
- J Cadzow and KOJI Ogino. Two-dimensional spectral estimation. *IEEE Transactions on Acoustics, Speech, and Signal Processing*, 29(3):396–401, 1981.
- X-D Zhang. On the estimation of two-dimensional moving average parameters. *IEEE Transactions on Automatic Control*, 36(10):1196–1199, 1991.
- Abdelhak M Zoubir, Visa Koivunen, Esa Ollila, and Michael Muma. *Robust statistics for signal processing*. Cambridge University Press, New York, USA, 2018.
- Edward J Wegman, Stuart C Schwartz, and John Bowman Thomas. *Topics in non-Gaussian signal processing*. Springer, New York, USA, 1989.
- Kaiguang Zhao, Sorin Popescu, and Xuesong Zhang. Bayesian learning with Gaussian processes for supervised classification of hyperspectral data. *Photogrammetric Engineering & Remote Sensing*, 74(10):1223–1234, 2008.
- Bei Zhao, Yanfei Zhong, Ailong Ma, and Liangpei Zhang. A spatial Gaussian mixture model for optical remote sensing image clustering. *IEEE Journal of Selected Topics in Applied Earth Observations and Remote Sensing*, 9(12):5748–5759, 2016.
- Pablo Morales-Alvarez, Adrián Pérez-Suay, Rafael Molina, and Gustau Camps-Valls. Remote sensing image classification with large-scale Gaussian processes. *IEEE Transactions on Geoscience and Remote Sensing*, 56(2):1103–1114, 2017.
- Steven M Kay. Can detectability be improved by adding noise? *IEEE Signal Processing Letters*, 7(1):8–10, 2000.
- Jian Xue, Shuwen Xu, and Penglang Shui. Near-optimum coherent CFAR detection of radar targets in compound-Gaussian clutter with inverse Gaussian texture. *Signal Processing*, 166:107236, 2020.
- Gang Wang, Carlos Lopez-Molina, Guillermo Vidal-Diez de Ulzurrun, and Bernard De Baets. Noise-robust line detection using normalized and adaptive second-order anisotropic Gaussian kernels. *Signal Processing*, 160:252–262, 2019.
- Argin Margoosian, Jamshid Abouei, and Konstantinos N Plataniotis. An accurate kernelized energy detection in Gaussian and non-Gaussian/impulsive noises. *IEEE Transactions on Signal Processing*, 63(21):5621–5636, 2015.
- Jun Liu, Sha Liu, Weijian Liu, Shenghua Zhou, Shengqi Zhu, and Zi-Jing Zhang. Persymmetric adaptive detection of distributed targets in compound-Gaussian sea clutter with Gamma texture. *Signal Processing*, 152:340–349, 2018.
- F. M. Bayer, D. M. Bayer, A. Marinoni, and P. Gamba. A novel Rayleigh dynamical model for remote sensing data interpretation. *IEEE Transactions on Geoscience and Remote Sensing*, 58(7):4989 – 4999, 2020a.
- Massimo Zanetti, Francesca Bovolo, and Lorenzo Bruzzone. Rayleigh-rice mixture parameter estimation via EM algorithm for change detection in multispectral images. *IEEE Transactions on Image Processing*, 24(12):5004–5016, 2015.

- Mohammed Naina Sumaiya and Ramapackiam Shantha Selva Kumari. Unsupervised change detection of flood affected areas in SAR images using Rayleigh-based Bayesian thresholding. *IET Radar, Sonar & Navigation*, 12(5):515–522, 2018.
- Dong-Xiao Yue, Feng Xu, Alejandro C Frery, and Ya-Qiu Jin. A generalized Gaussian coherent scatterer model for correlated SAR texture. *IEEE Transactions on Geoscience and Remote Sensing*, 58(4), 2019.
- Ercan E Kuruoglu and Josiane Zerubia. Modeling SAR images with a generalization of the Rayleigh distribution. *IEEE Transactions on Image Processing*, 13(4):527–533, 2004.
- Julie Ann Jackson and Randolph L Moses. A model for generating synthetic VHF SAR forest clutter images. *IEEE Transactions on Aerospace and Electronic Systems*, 45(3):1138 – 1152, 2009.
- Shyam Kuttikkad and Rama Chellappa. Statistical modeling and analysis of high-resolution synthetic aperture radar images. *Statistics and Computing*, 10(2):133–145, 2000.
- Chris Oliver and Shaun Quegan. *Understanding synthetic aperture radar images*. SciTech Publishing, USA, 2004.
- Dong-Xiao Yue, Feng Xu, Alejandro C. Frery, and Ya-Qiu Jin. Synthetic aperture radar image statistical modeling: Part one-single-pixel statistical models. *IEEE Geoscience and Remote Sensing Magazine*, 9(1):82–114, 2021.
- Haipeng Wang and Kazuo Ouchi. Accuracy of the k -distribution regression model for forest biomass estimation by high-resolution polarimetric SAR: Comparison of model estimation and field data. *IEEE Transactions on Geoscience and Remote Sensing*, 46(4):1058–1064, 2008.
- P. McCullagh and J.A. Nelder. *Generalized linear models*. Chapman and Hall, New York, USA, 2nd edition, 1989.
- Bruna G Palm, Fábio M Bayer, Renato J Cintra, Mats I Pettersson, and Renato Machado. Rayleigh regression model for ground type detection in SAR imagery. *IEEE Geoscience and Remote Sensing Letters*, 16(10):1660 – 1664, 2019.
- Hao Yan, Kamran Paynabar, and Jianjun Shi. Real-time monitoring of high-dimensional functional data streams via spatio-temporal smooth sparse decomposition. *Technometrics*, 60(2):181–197, 2018.
- Pedro M Almeida-Junior and Abraão DC Nascimento. G_i^0 ARMA process for speckled data. *Journal of Statistical Computation and Simulation*, 2021. doi: 10.1080/00949655.2021.1922688.
- Michael A Benjamin, Robert A Rigby, and D Mikis Stasinopoulos. Generalized autoregressive moving average models. *Journal of the American Statistical Association*, 98(461):214–223, 2003.
- Fábio Mariano Bayer, Débora Missio Bayer, and Guilherme Pumi. Kumaraswamy autoregressive moving average models for double bounded environmental data. *Journal of Hydrology*, 555:385–396, 2017.
- A. V. Rocha and F. Cribari-Neto. Beta autoregressive moving average models. *Test*, 18(3):529–545, 2009.
- Tobias A Möller and Christian H Weiß. Generalized discrete autoregressive moving-average models. *Applied Stochastic Models in Business and Industry*, 36(4):641–659, 2020.
- Bruna G. Palm, Fábio M. Bayer, and Renato J. Cintra. Signal detection and inference based on the beta binomial autoregressive moving average model. *Digital Signal Processing*, 109:102911, 2021.
- Débora M Bayer, Fábio M Bayer, and Paolo Gamba. A 3-D spatiotemporal model for remote sensing data cubes. *IEEE Transactions on Geoscience and Remote Sensing*, 52(2):1082–1093, 2020b.
- Evan B Brooks, Randolph H Wynne, Valerie A Thomas, Christine E Blinn, and John W Coulston. On-the-fly massively multitemporal change detection using statistical quality control charts and Landsat data. *IEEE Transactions on Geoscience and Remote Sensing*, 52(6):3316–3332, 2013.
- Priyanga Dilini Talagala, Rob J Hyndman, and Kate Smith-Miles. Anomaly detection in high-dimensional data. *Journal of Computational and Graphical Statistics*, 30(2):360–374, 2020.
- Farid Kadri, Fouzi Harrou, Sondès Chaabane, Ying Sun, and Christian Tahon. Seasonal ARMA-based SPC charts for anomaly detection: Application to emergency department systems. *Neurocomputing*, 173:2102–2114, 2016.
- Elena Quatrini, Francesco Costantino, Giulio Di Gravio, and Riccardo Patriarca. Machine learning for anomaly detection and process phase classification to improve safety and maintenance activities. *Journal of Manufacturing Systems*, 56:117–132, 2020.
- Heesung Kwon and Nasser M Nasrabadi. Kernel RX-algorithm: A nonlinear anomaly detector for hyperspectral imagery. *IEEE Transactions on Geoscience and Remote Sensing*, 43(2):388–397, 2005.
- Cristiane Melchior, Roselaine Ruviaro Zanini, Renata Rojas Guerra, and Dinei A Rockenbach. Forecasting Brazilian mortality rates due to occupational accidents using autoregressive moving average approaches. *International Journal of Forecasting*, 37(2):825–837, 2021.

- Víctor Leiva, Helton Saulo, Rubens Souza, Robert G Aykroyd, and Roberto Vila. A new BISARMA time series model for forecasting mortality using weather and particulate matter data. *Journal of Forecasting*, 40(2):346–364, 2020.
- Ella R Rothermel, Matthew T Balazik, Jessica E Best, Matthew W Breece, Dewayne A Fox, Benjamin I Gahagan, Danielle E Haulsee, Amanda L Higgs, Michael HP O’Brien, Matthew J Oliver, et al. Comparative migration ecology of striped bass and Atlantic sturgeon in the US Southern mid-Atlantic bight flyway. *PloS One*, 15(6):e0234442, 2020.
- Tobias Liboschik, Konstantinos Fokianos, and Roland Fried. tscount: An R package for analysis of count time series following generalized linear models. *Journal of Statistical Software*, 82(1):1–51, 2017.
- Vinícius T Scher, Francisco Cribari-Neto, Guilherme Pumi, and Fábio M Bayer. Goodness-of-fit tests for β ARMA hydrological time series modeling. *Environmetrics*, 31(3):e2607, 2020.
- W. Press, S. Teukolsky, W. Vetterling, and B. Flannery. *Numerical recipes in C: The art of scientific computing*. Cambridge University Press, New York, USA, 2nd edition, 1992.
- J. Nocedal and S. J. Wright. *Numerical optimization*. Springer, New York, USA, 1999.
- R. C. Mittelhammer, G. G. Judge, and D. J. Miller. *Econometric Foundations*. Cambridge University Press, Cambridge, UK, 2000.
- Erling Bernhard Andersen. Asymptotic properties of conditional maximum-likelihood estimators. *Journal of the Royal Statistical Society: Series B (Methodological)*, 32(2):283–301, 1970.
- Y. Pawitan. *In all likelihood: Statistical modelling and inference using likelihood*. Oxford Science publications, UK, 2001.
- Steven M. Kay. *Fundamentals of statistical signal processing: Detection theory*, volume II. Prentice Hall, Upper Saddle River, NJ, USA, 1998.
- Benjamin Kedem and Konstantinos Fokianos. *Regression models for time series analysis*. John Wiley & Sons, New Jersey, USA, 2005.
- Peter K. Dunn and Gordon K. Smyth. Randomized quantile residuals. *Journal of Computational and Graphical Statistics*, 5(3):236–244, 1996.
- Fábio M Bayer, Alice J Kozakevicius, and Renato J Cintra. An iterative wavelet threshold for signal denoising. *Signal Processing*, 162: 10–20, 2019.
- J Edmond, J Ronald, and T Hugues. Mathematical morphology: A useful set of tools for image analysis. *Statistics and Computing*, 10(2): 105–120, 2000.
- R Gonzalez, R Woods, and S Eddine. Digital image processing using MATLAB, 2009.
- G. Box, G. M. Jenkins, and G. Reinsel. *Time series analysis: Forecasting and control*. Hardcover, John Wiley & Sons, USA, June 2008.
- Hirotsugu Akaike. A new look at the statistical model identification. *IEEE Transactions on Automatic Control*, 19(6):716–723, 1974.
- Gideon Schwarz et al. Estimating the dimension of a model. *The Annals of Statistics*, 6(2):461–464, 1978.
- Mikael Lundberg, Lars M. H. Ulander, William E. Pierson, and Anders Gustavsson. A challenge problem for detection of targets in foliage. In *Proc. SPIE*, volume 6237, page 62370K, 2006.
- Lars MH Ulander, M Lundberg, W Pierson, and A Gustavsson. Change detection for low-frequency SAR ground surveillance. *IEEE Proceedings-Radar, Sonar and Navigation*, 152(6):413–420, 2005.
- Viet Thuy Vu, Natanael Rodrigues Gomes, Mats I Pettersson, Patrik Dammert, and Hans Hellsten. Bivariate gamma distribution for wavelength-resolution SAR change detection. *IEEE Transactions on Geoscience and Remote Sensing*, 57(1):473–481, 2018.
- Viet Thuy Vu. Wavelength-resolution SAR incoherent change detection based on image stack. *IEEE Geoscience and Remote Sensing Letters*, 14(7):1012–1016, 2017.
- Renato J Cintra, Alejandro C Frery, and Abraao DC Nascimento. Parametric and nonparametric tests for speckled imagery. *Pattern Analysis and Applications*, 16(2):141–161, 2013.
- Bahram Safaei and Mahmod Reza Sahebi. A class-based approach to classify PolSAR imagery using optimum classifier. *European Journal of Remote Sensing*, 52(1):294–307, 2019.
- Abraão DC Nascimento, Michelle M Horta, Alejandro C Frery, and Renato J Cintra. Comparing edge detection methods based on stochastic entropies and distances for PolSAR imagery. *IEEE Journal of Selected Topics in Applied Earth Observations and Remote Sensing*, 7(2):648–663, 2013.
- Luis Gomez, Luis Alvarez, Luis Mazorra, and Alejandro C Frery. Fully PolSAR image classification using machine learning techniques and reaction-diffusion systems. *Neurocomputing*, 255:52–60, 2017.